GEOPHYSICS, VOL. 62, NO. 1 (JANUARY-FEBRUARY 1997); P. 253–265, 12 FIGS.

Diffraction of seismic waves by cracks with application to hydraulic fracturing

Enru Liu*, Stuart Crampin‡, and John A. Hudson**

ABSTRACT

We describe a method of modeling seismic waves interacting with single liquid-filled large cracks based on the Kirchhoff approximation and then apply it to field data in an attempt to estimate the size of a hydraulic fracture. We first present the theory of diffraction of seismic waves by fractures using a Green's function representation and then compute the scattered radiation patterns and synthetic seismograms for fractures with elliptical and rectangular shapes of various dimensions. It is shown that the characteristics of the diffracted wavefield from single cracks are sensitive to both crack size and crack shape. Finally, we compare synthetic waveforms to observed waveforms recorded during a hydraulic fracturing experiment and are able to predict successfully the size of a hydraulically induced fracture (length and height). In contrast to previously published work based on the Born approximation, we model both phases and amplitudes of observed diffracted waves. Our modeling has resulted in an estimation of a crack length 1.1 to 1.5 times larger than previously predicted, whereas the height remains essentially the same as that derived using other techniques. This example demonstrates that it is possible to estimate fracture dimensions by analyzing diffracted waves.

INTRODUCTION

Hydraulic fracturing for enhancing the recovery of hydrocarbons has become a common reservoir engineering practice, and the geometry of the induced fractures is critically important for their efficacy in production (Vinegar et al., 1992; Wills et al., 1992; Meadows and Winterstein, 1994). Various methods have been used to estimate the size of fractures. The most successful one has been the shear-wave shadow method. There are several field examples of shear-wave shadowing, such as Fehler and Pearson, 1984; Niitsuma and Saito, 1991; and Wills et al., 1992. However, this method is only applicable when there is a wide range of raypaths across the end of the fracture. Recently, Meadows and Winterstein (1994) provided a comprehensive review of seismic contributions in detecting and locating fractures, and suggested an alternative method for estimating the size of hydraulic fractures by modeling observed diffracted wavelets.

In this paper, we model the diffracted response of seismic waves from 3-D cracks numerically using the Kirchhoff approximation (Douglas and Hudson, 1990; Raynaud, 1988). Several other methods are also available for treating diffraction problems: integral representations (van der Hijden and Neerhoff, 1984a, b); discrete wavenumber techniques (Coutant, 1989); generalized ray techniques (Achenbach et al., 1982); finite-difference methods (FDM) (Fehler and Aki, 1978); the finite-element method (FEM); and boundary element methods (BEM) (Chen and Zhou, 1994). The advantages of the Kirchhoff approximation over other techniques lie in its simplicity, fast computing speed, and accuracy. We compute the scattered radiation patterns of seismic waves incident on fluid-filled circular cracks and show the corresponding synthetic seismograms for some simple models to demonstrate the effects of single cracks on the seismic response.

Next, we compare the synthetic waveforms to the observed waveforms from a field data set in an attempt to estimate the size of a hydraulic fracture. The field data were recorded continuously over a period of about two hours during a hydraulic fracturing experiment and were analyzed by Meadows and Winterstein (1994). The diffracted wavefield associated with the hydraulic fracture was isolated simply by the subtraction of recorded traces from a reference trace. The data show a clear variation of waveform properties (amplitude and phase) as a function of time—a direct observation of the evolution of cracks. This wave behavior has significant implications for improved oil recovery.

Meadows and Winterstein (1994) attempted to estimate the size of the fracture by using the Born approximation of Wu and

Manuscript received by the Editor January 11, 1995; revised manuscript received April 10, 1996.
*British Geological Survey, Murchison House, West Mains Road, Edinburgh EH9 3LA, United Kingdom.
‡Department of Geology and Geophysics, University of Edinburgh, West Mains Road, Edinburgh EH9 3JW, United Kingdom.
**Department of Applied Mathematics and Theoretical Physics, University of Cambridge, Silver Street, Cambridge CB3 9EW, United Kingdom.

Aki (1985) to match the recorded diffracted waveforms. However, they were only able to match adequately the phases of the recorded wavelets. The amplitudes of their synthetic waveforms are too small in comparison with the recorded wavelets since the Born approximation is only valid for weak scattering (Hudson and Heritage, 1981; Wu and Aki, 1985). In this paper, we use the Kirchhoff approximation, which is valid for large-scale scatterers and thus more appropriate to tackle fracture-related diffraction problems to model both the amplitudes and phases of observed waveforms. Our modeling has resulted in the estimation of a crack length about 1.1 to 1.5 times larger than previously predicted, whereas the height remains essentially the same as that derived using other techniques. This example demonstrates that careful analysis and modeling can provide accurate information about the dimensions of hydraulic fractures.

THE KIRCHHOFF REPRESENTATION OF THE SCATTERED WAVEFIELD

In the presence of cracks, the total wavefield can be written as

$$u_i(\mathbf{x}) = u_i^0(\mathbf{x}) + u_i^s(\mathbf{x}), \tag{1}$$

where u_i^0 is the ith component of the incident wavefield (the wavefield in the absence of the scatterer), and u_i^s is the ith component of the scattered wave at point $\mathbf{x}$. Using Green's function, Hudson (1980) and Aki and Richards (1980) give an expression for the seismic radiation from sources distributed over the surface of an internal crack or discontinuity, i.e., u_i^s is represented as a surface integral

$$u_i^s(\mathbf{x}) = -\int_\Sigma [u_k(\mathbf{X})] c_{kjpq}^0 \frac{\partial G_i^p(\mathbf{x}, \mathbf{X})}{\partial x_q} n_j \, dS_X, \tag{2}$$

where n_j is the jth component of the normal $\mathbf{n}$ to the crack surface Σ, $\mathbf{X}$ is a point on the crack face, $[u_k]$ is the kth displacement discontinuity across the crack in the direction of $\mathbf{n}$ (crack normal), and c_{kjpq}^0 is the elastic tensor of the matrix solid, which is assumed to be isotropic in this study, and is given by

$$c_{kjpq}^0 = \lambda \delta_{kj}\delta_{pq} + \mu(\delta_{kp}\delta_{jq} + \delta_{kq}\delta_{jp}), \tag{3}$$

where λ and μ are the Lamé constants, and δ_{ij} is the Kronecker delta. The Green's function $G_i^p(\mathbf{x}, \mathbf{X})$ is the ith component of displacement at $\mathbf{x}$ because of a unit force in the pth direction at $\mathbf{X}$, and for an isotropic full-space model is

$$G_i^p(\mathbf{x}, \mathbf{X}) = \frac{1}{4\pi\rho}\left[\frac{\ell_i \ell_p}{\alpha^2 r} e^{i\omega r/\alpha} + \frac{(\delta_{ip} - \ell_i \ell_p)}{\beta^2 r} e^{i\omega r/\beta}\right], \tag{4}$$

ignoring the near-field contribution, where ω is the angular frequency, ρ is the density, α and β are the P- and S-wave speeds, respectively, and

$$r = |\mathbf{x} - \mathbf{X}|,$$

and

$$\mathbf{l} = \frac{(\mathbf{x} - \mathbf{X})}{r}. \tag{5}$$

Equation (2) provides a means of evaluating the scattered field so long as the displacement discontinuity $[\mathbf{u}]$ on the crack can be estimated accurately. The amplitudes and phases of $[\mathbf{u}]$ are unknown; in the Kirchhoff approximation, these are taken to be the same as if the crack were infinitely long; that is, the effect of the boundary is ignored.

If the incident wave is a plane wave of the form

$$u_i^0 = q_i \, e^{i\mathbf{k}\cdot\mathbf{x}}, \tag{6}$$

then $[u_i]$ can be approximately expressed as

$$[u_i] = Q_i e^{i\mathbf{k}\cdot\mathbf{X}}, \tag{7}$$

for point $\mathbf{X}$ on the crack face, where $\mathbf{k}$ is the wavenumber vector, and the displacement discontinuity Q_i is independent of $\mathbf{X}$ and is derived in the Appendix.

Putting equations (4) and (7) into equation (2), the far-field expression for u_i^s can be divided into two parts: a scattered P-wave

$$^P u_i^s(\mathbf{x}) = -c_{kjpq}^0 Q_k n_j \frac{i\omega}{4\pi\rho\alpha^3} \times \int_\Sigma \ell_i \ell_p \ell_q \frac{e^{i\omega r/\alpha + i\mathbf{k}\cdot\mathbf{X}}}{r} \, dS_X, \tag{8}$$

and a scattered S-wave

$$^S u_i^s(\mathbf{x}) = -c_{kjpq}^0 Q_k n_j \frac{i\omega}{4\pi\rho\beta^3} \times \int_\Sigma (\delta_{ip} - \ell_i \ell_p)\ell_q \frac{e^{i\omega r/\beta + i\mathbf{k}\cdot\mathbf{X}}}{r} \, dS_X. \tag{9}$$

Equations (8) and (9) are valid for any shape of crack. They can be simplified further if the distance from the crack is large compared with the size of the crack. For a circular crack of radius a, Hudson et al. (1996) obtained the analytic solutions for the far-field displacements, which are for P- and S-waves, respectively

$$^P \mathbf{u}^s(\mathbf{x}) = D_p \mathbf{l}^0 \left[\frac{\lambda}{\lambda + 2\mu} Q_3 + \frac{2\mu}{\lambda + 2\mu}(\mathbf{Q}\cdot\mathbf{l}^0)\ell_3^0\right], \tag{10}$$

and

$$^S \mathbf{u}^s(\mathbf{x}) = D_s\left[\ell_3^0 \mathbf{Q} + \mathbf{e}_3(\mathbf{Q}\cdot\mathbf{l}^0) - 2\mathbf{l}^0 \ell_3^0 (\mathbf{Q}\cdot\mathbf{l}^0)\right], \tag{11}$$

where the coefficients D_p and D_s are

$$D_p = -\left(\frac{\omega a^2}{\alpha r^0}\right)\left(\frac{i}{2}\right)\frac{J_1(\sigma_\alpha a)}{\sigma_\alpha a} e^{\frac{i\omega r^0}{\alpha}}, \tag{12}$$

and

$$D_s = -\left(\frac{\omega a^2}{\beta r^0}\right)\left(\frac{i}{2}\right)\frac{J_1(\sigma_\beta a)}{\sigma_\beta a} e^{\frac{i\omega r^0}{\beta}}, \tag{13}$$

where

$$\begin{aligned}
\sigma_\alpha &= \left[|\mathbf{s}^\alpha|^2 - \left(s_3^\alpha\right)^2\right]^{1/2};\\
\sigma_\beta &= \left[|\mathbf{s}^\beta|^2 - \left(s_3^\beta\right)^2\right]^{1/2};\\
\mathbf{s}^\alpha &= \mathbf{k} - \mathbf{k}^\alpha;\\
\mathbf{s}^\beta &= \mathbf{k} - \mathbf{k}^\beta;\\
\mathbf{k}^\alpha &= (\omega/\alpha)\cdot\mathbf{l}^0;\\
\mathbf{k}^\beta &= (\omega/\beta)\cdot\mathbf{l}^0.
\end{aligned} \tag{14}$$

J_1 is the Bessel function of the first kind of first order, $\mathbf{e}_3 = (0, 0, 1)$ is the crack normal along the z-axis, r^0 is the distance between the centroid of the crack $\mathbf{X}^0$, the observation point $\mathbf{x}$, and $\mathbf{l}^0 = (\mathbf{x} - \mathbf{X}^\mathbf{0})/\mathbf{r}^\mathbf{0}$.

MODELING DIFFRACTION BY CRACKS

The Kirchhoff approximation is assumed to be valid for dimensionless ka greater than about 3 (Hudson et al., 1996). The displacements of scattered waves are calculated in the local coordinate system, that is, with the normal of the fracture along the z-axis, and x and y in the plane of cracks. A rotation will transform the displacements from the local coordinate system to the global coordinate system for a general 3-D crack configuration. The integrals in equations (8) and (9) can be easily evaluated numerically by a Gaussian quadrature formulation (modified from Press et al., 1992). Moreover, the accuracy is guaranteed by the choice of a sufficiently small integration step.

Scattered radiation patterns

The scattered far-field radiation patterns in Figure 1 show the response of incident plane P- and SV-waves scattered from circular cracks filled with water. The computation was carried out for $ka = 3$ and 6 with a Poisson's ratio of 1/3 for the background solid (a P- to S-wave velocity ratio of 2, therefore $k_\beta = 2k_\alpha$). Each radiation pattern shows the angular variation in scattering displacements. For each diagram, the left column corresponds to an incident P-wave and the right column to an incident SV-wave. Solid lines are scattered P-waves and dashed lines are scattered SV-waves. The calculation was performed for four incident angles θ (0°, 30°, 60°, and 90° measured from the crack normal). Except when the incident angle θ is close to 0°, forward scattered energy is dominant. Comparing the scattered diagrams with those of a 2-D dry crack (van der Hijden and Neerhoff, 1984a), we find that they both give similar angular patterns.

Effects of a single circular crack

Figure 2 gives the model geometry for the transmission and diffraction of seismic waves from a single circular crack in the sagittal plane. In the following computations, the uncracked matrix solid is assumed to be isotropic with P- and S-wave velocities $\alpha = 3.5$ and $\beta = 2.0$ km/s, respectively, and density

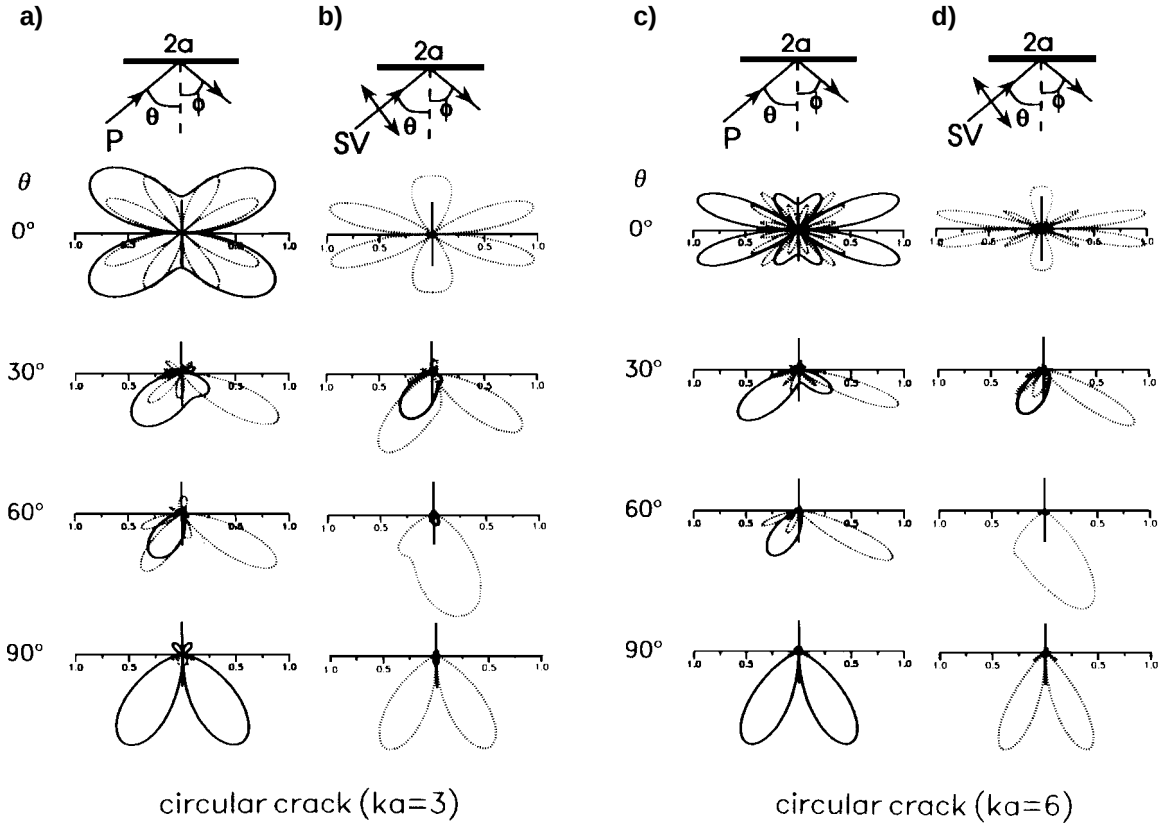

FIG. 1. Scattered far-field radiation patterns for circular cracks with $ka = 3$ and $ka = 6$ using the Kirchhoff approximation. The solid lines are for P-waves, and the dashed lines are for SV-waves. The incident angle θ is measured from the crack normal.

$\rho = 2.3\,\mathrm{g/cm^3}$. The source is a point force aligned at 45° between horizontal transverse SH- and radial SV-directions, and it will excite all three body waves in the sagittal plane. The water-filled crack has an opening of 1 cm and a radius of 15 m. To assist in the identification of various diffracted arrivals in the synthetic seismograms, the traveltimes calculated by conventional ray theory are shown in Figures 3a and 3b. All waves in the transverse (or T) components are SH-type waves and are not explicitly referred in the following discussion. Since S-waves are more sensitive to the presence of cracks than P-waves (Crampin, 1985), we shall focus our analysis on the S-waves with only occasional reference to P-waves.

Figure 4a shows the complete three-component synthetic seismograms generated for the model in Figure 2, with a peak source frequency of 200 Hz (thus, $k_\alpha a = 5.4$, and $k_\beta a = 9.4$, or equivalently a wavelength/crack radius ratio of 1.16 and 0.67 for P- and S-waves, respectively). R, T, and V refer to the radial, transverse, and vertical components, respectively, as defined in Figure 2. All traces are plotted with true relative amplitudes unless specified otherwise. For comparison of relative amplitudes, Figure 4b shows the synthetic seismograms without the crack, and Figure 4c shows only the diffracted arrivals computed using the same source-receiver geometry. Different arrivals corresponding to the traveltime plots in Figure 4 can be identified using the various line types identified in Figure 3b. Only S-to-S and S-to-P wave traveltimes are drawn in Figure 4. The earlier P-to-P and P-to-S waves are not marked. The traveltimes of these expected diffracted arrivals are in good agreement with the curves in Figure 3 computed from standard ray theory. Traveltime plots, such as those in Figure 3, have proved to be useful in identifying wave types. The interference of scattered waves and fracture interface waves (Gu et al., 1996) with direct waves is clearly evident, particularly for the geophones on the right-hand side of the model where the traveltimes for various arrivals are close together. As a result of this interference pattern, the amplitudes in the middle traces (immediately below the crack) are diminished and there is a slight time lag (Figure 4a). The diffracted waves in Figure 4c are replotted in Figure 5 by subtracting the traces in Figure 4b from Figure 4a (the dashed lines will be discussed later). The waveforms are relatively simple and vary for different geophone locations. In particular, for the middle geophones, the waveforms are simpler than for geophones on either side of the model because of the interference pattern produced by the various diffracted arrivals.

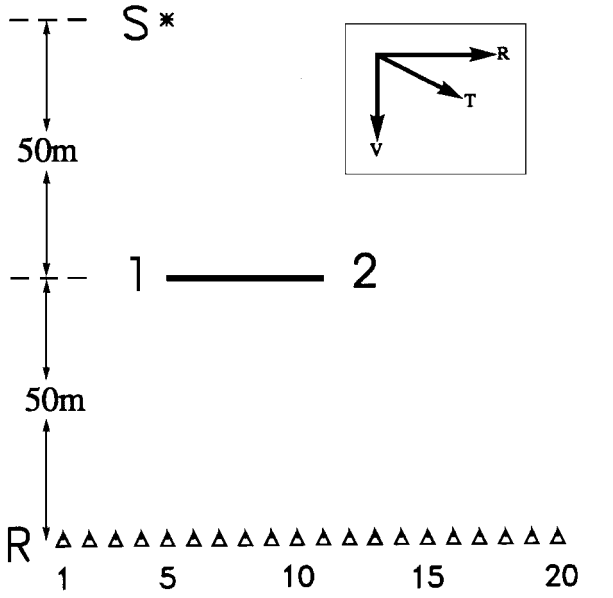

FIG. 2. Source-medium-receiver configuration used for calculating synthetic seismograms. The thick solid line in the middle denotes a water-filled circular crack with two edges marked 1 and 2, respectively. The source (S) is 50 m above the crack and the line of receiver (R) at 5 m spacing is 50 m below the crack. Radial, transverse, and vertical components are defined at the top right of the figure.

Effects of shapes: Elliptical and rectangular cracks

Figure 5 compares the scattered waveforms for circular cracks (solid lines) with those for square cracks (dashed line). The diameter of the circular crack is the same as the side of

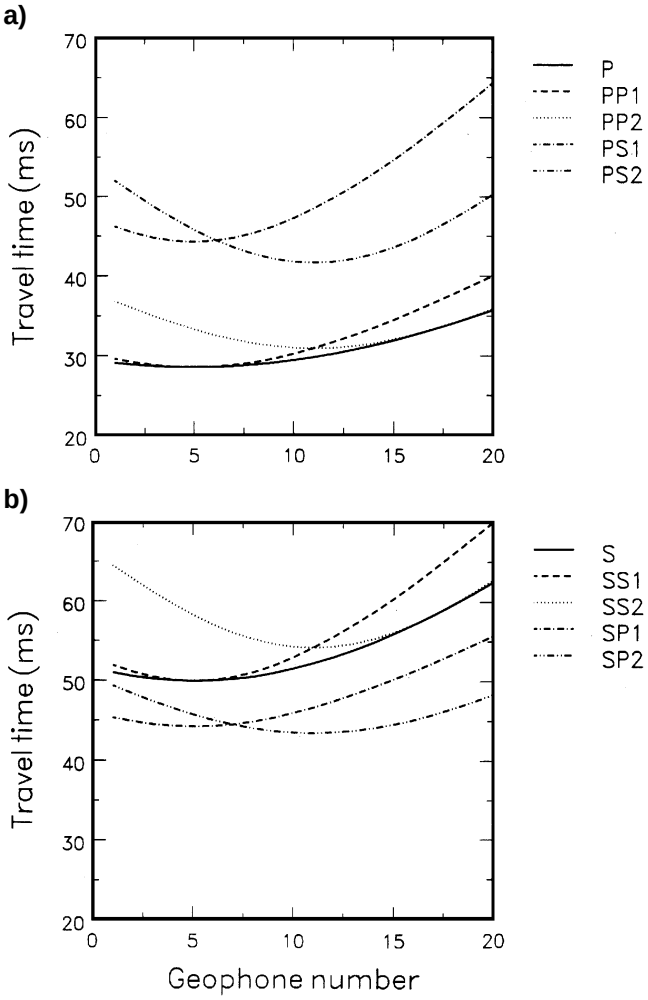

FIG. 3. Ray theoretical traveltimes for diffracted waves according to the model geometry in Figure 2. (a) P-wave incidence, and (b) S-wave incidence. The labels can be identified as follows: for example, PP_i refers to a P-wave generated by a P source and diffracted from the crack edge i; similarly, PS_i is an S-wave generated by a P source and diffracted from the crack edge i; and P and S are direct P- and S-waves, respectively.

the square crack. The model used is the same as that shown in Figure 2. In general, the forward scattered waveforms are similar (receivers 8 to 20), and the differences are principally in the back-scattered waveforms (receivers 1 to 7). Figure 6 shows the scattered waveforms for elliptical cracks with three different axis ratios $b = 2a, 5a$, and $10a$, where b is the long axis of the ellipse, and the short axis is $a = 15$ in the plane, as used in the previous examples. Only traces corresponding to receivers 1, 5, 10, 15, and 20 in Figure 2 are plotted. Amplitudes are vector normalized, so that the amplitudes for each group (R, T, and V) can be directly compared. Figure 7 shows a similar plot to Figure 6, but for rectangular cracks. Waveforms for elliptical cracks are quite different from those for rectangular cracks. One feature to note is that when the ratio b/a increases, more coda waves become visible. This is expected because scattered waves from crack boundaries will travel greater distances for a long crack than for a narrow crack, and therefore will form more pronounced coda waves. In addition, fracture interface waves may be generated (Gu et al., 1996). Another characteristic feature is that the amplitudes and phases of scattered waves vary with fracture size. This feature has been recognized by Meadows and Winterstein (1994), and will be used to estimate the dimensions of a hydraulically induced fracture in the next section.

APPLICATION TO FIELD DATA

The experiment and aim of this study

Meadows and Winterstein (1994) have described the data acquisition and processing in detail, and we repeat only the information that is relevant to this study. The data were recorded by Chevron in the Lost Hills production field. Figure 8 a shows the plan view of the three boreholes, and Figure 8b is a schematic illustration of the 3-D configuration of the source, geophones, and expected fracture position in the field experiment (not to scale). The Omnipulse® airgun source was located close to borehole 11-10X. VSP data were acquired in wells 11-10X and 1-8B by three-component geophones after the hydraulic fracturing treatment in well 12-10. The data were recorded for a period of nearly two hours. In Figure 8b, the shaded rectangular

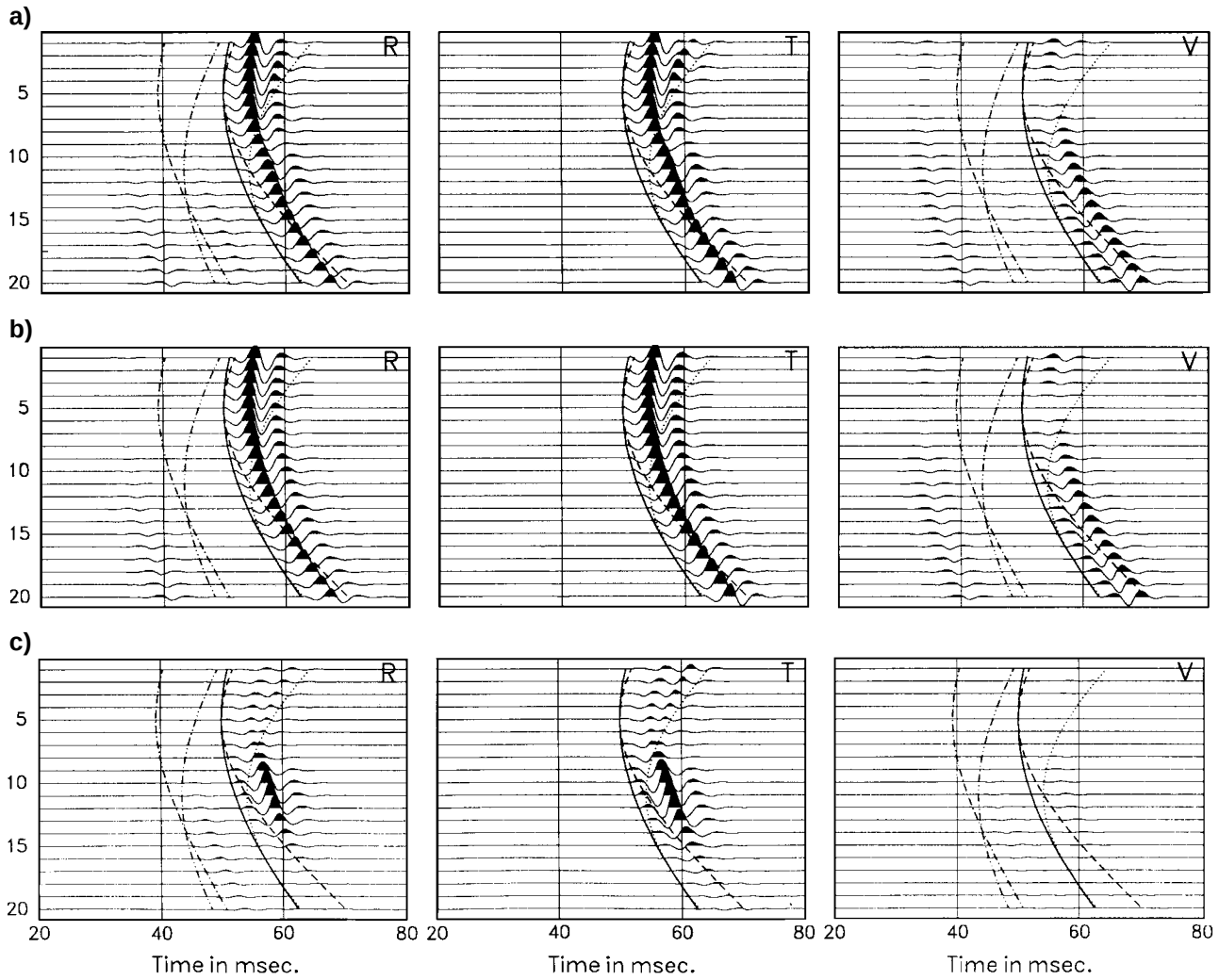

FIG. 4. Three-component synthetic seismograms corresponding to the model geometry in Figure 2: (a) with the crack, (b) without the crack, and (c) the scattered waves [(a − b)]. The ray traveltimes in Figure 3 are marked for identification. The numbers on the left correspond to geophone numbers in Figure 2.

area represents the expected hydraulic fracture, which is assumed to be symmetric about the borehole. The angle θ is the fracture deviation from the vertical, and ϕ is the fracture strike direction relative to the plane containing boreholes 1-8B and 11-10X, which is also believed to be the direction of the local maximum compressional stress. The aim of this experiment was to compare data recorded before fracturing with data recorded after fracturing at identical depths and geophone orientations. In this way, any changes seen in the data after fracturing could only be attributed to the fractures themselves, and not to differences in recording.

Meadows and Winterstein modeled the phase of diffracted waves successfully using the Born approximation. However, the amplitudes from the Born approximation are too small in comparison with the observed amplitudes of the diffracted waves. Here, we reanalyze the data and attempt to use the Kirchhoff approximation to model both the amplitude and phase of the observed diffracted waves to obtain fracture size (length and height).

Data analysis and summary of previous results by Meadows and Winterstein

In this section, we summarize the results obtained by Meadows and Winterstein (1994) for their analysis of the diffracted wavefields. They found that the vertical seismic profile (VSP) data recorded in well 11-10X before and after hydraulic fracturing showed very little difference, whereas the data recorded in well 1-8B showed transient effects on all four components. These variations with time diminish over about one hour, after which the waveforms return to those observed before the hydraulic fracture. After a four-component Alford rotation (Tatham and McCormack, 1991, 156), the transient effects are clearly seen to be confined to the shear waves on the slower XX-components, whereas the faster YY-components show little variation. The transient effects seen on the XX-component are a direct consequence of the fracturing and imply that the process principally affects the shear waves which are polarized perpendicular to the fractures for the geometry of this experiment.

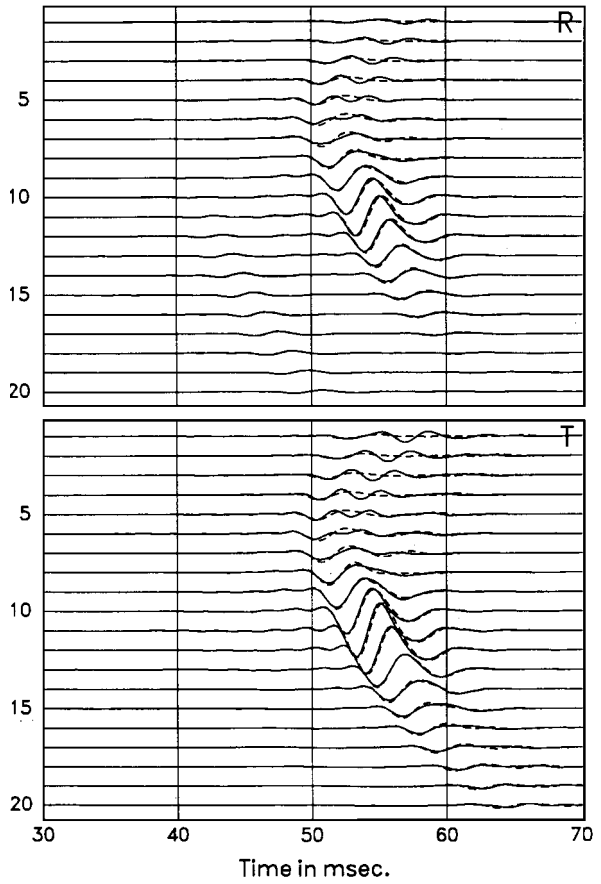

FIG. 5. Comparison of scattered waveforms for a circular crack (solid lines) that is an enlargement of Figure 4c, and a square crack (dashed lines). Model geometry as in Figure 2. The numbers on the vertical axis correspond to the geophone numbers in Figure 2.

The obvious explanation of the anomalies seen in the 1-8B data is that the seismic waves which traveled from the source near well 11-10X interacted with the hydraulic fractures induced from the well 12-10 situated between 1-8B and 11-10X (Figure 8a) and became distorted, whereas the backscattered 11-10X data were unaffected. Meadows and Winterstein (1994) interpreted the transient effects from the waves polarized perpendicular to the fractures as comprising two overlapping signals: a direct arrival and a wavelet diffracted from the fracture that arrives a short time later (approximate raypaths are given in Figure 8b). As the fracture closes, it becomes increasingly transparent to the incident wave and the scattered energy disappears.

To isolate the diffracted waves, a simple trace differencing technique was applied; the last recorded waveforms are taken to represent the reference wavelet, and are subtracted from the remaining waveforms. The results are reproduced in Figure 9 for the XX-components (after Meadows and Winterstein). From Figure 9, it can be seen clearly that the diffracted energy disappears within about an hour after the shut-in. In addition, the arrival time of the residual wavelets consistently lags behind that of the direct arrivals by about a half period (25 ms). The residual wavelets are smaller in amplitude than the incident wavelet and display very little of the wavelet broadening present before subtraction. The residual wavelets, however, are not simply the duplicate of the incident waves, but appear to be slightly phase-rotated.

A Born approximation (Wu and Aki, 1985) was used by Meadows and Winterstein (1994) to match the waveforms of the diffracted waves. The fracture was modeled as a rectangular surface of point scatters. The scattered waves from each point scatter are then summed to obtain the total scattered waves. Though they are able to match the phase of the diffracted waves well by adjusting the size of the initially predicted fracture, the amplitudes of the scattered waves are not adequately matched. Meadows and Winterstein also find that the phase is not sensitive enough to the fracture size to obtain any decisive results. They finally estimate that the fracture length is no more than half of the predicted propped length (173 m) and the height is no more than twice the predicted propped height (66 m). The predicted propped height $H_{\text{predicted}} = 66$ m is measured from radioactive tracers, and the predicted propped length $L_{\text{predicted}} = 170$ m is calculated from the Kristianovich-Geertsma-deKlerk 2-D model (Geertsma and deKlerk, 1969). Note that YY-components, or SH-waves polarized parallel to the fracture, were not modeled by Meadows

and Winterstein, nor did they show any residual arrivals from the YY-component as they did in Figure 9 for XX-components or SV-waves polarized perpendicular to the fracture, since this energy was deemed to be insignificant.

Results from applying the Kirchhoff approximation

According to Meadows and Winterstein, the dominant signal frequency is 19 Hz, and the average shear-wave velocity near the receiver is about 696 m/s. It is implied that $k_\beta a = 5.7$ if we use their fracture height of 66 m, so the wavenumber requirement for the applicability of the Kirchhoff approximation is satisfied.

The source function used in the synthetic modeling is a zero-phase wavelet defined as

$$f(t) = e^{-\omega t/d} \sin(\omega t), \tag{15}$$

where d is a damping factor, and $d = 3$ is used in this modeling. This pulse is used in order to simulate the wavelet recorded before the hydraulic fracturing treatment, and is similar to that used by Meadows and Winterstein in their modeling.

Figures 10 to 12 show several sets of modeled waveforms illustrating the effects of fracture size (height and length of a rectangular fracture) on the amplitudes and phases. The first trace in all plots is the input wavelet. The numbers on the right side of the plots indicate fracture height (first number) and length (second number). Figure 10 shows the variation in waveforms with fracture length, for a fixed height [as predicted by engineers using other methods, see Meadows and Winterstein (1994), Table 3], where the fracture is assumed to be parallel to the source and geophone. Figure 11 shows a similar plot to Figure 10, but "true" fracture orientations estimated by Meadows and Winterstein are considered as shown in Figure 8b, i.e., $\theta = 7^\circ$ and $\phi = 3^\circ$ [given in Meadows and Winterstein (1994), Table 3]. The amplitudes and waveforms of synthetic scattered waves vary significantly with fracture length, whereas the change in phase is less pronounced. We suggest that the fracture height can be well predicted in the field (as it is probably controlled by local lithology), but estimates of the length are usually less accurate. If we assume that the fracture height predicted by engineers (cited by Meadows and Winterstein) is correct, and model the subtle difference in phase between the first two peaks of the scattered waves, then we obtain a fracture length of about 200 to 250 m (traces 6 and 7 in Figure 11), that is, about 1.1 to 1.5 times the estimated value of 170 m. Figure 12 shows a series of waveforms for various fracture heights with a fixed length

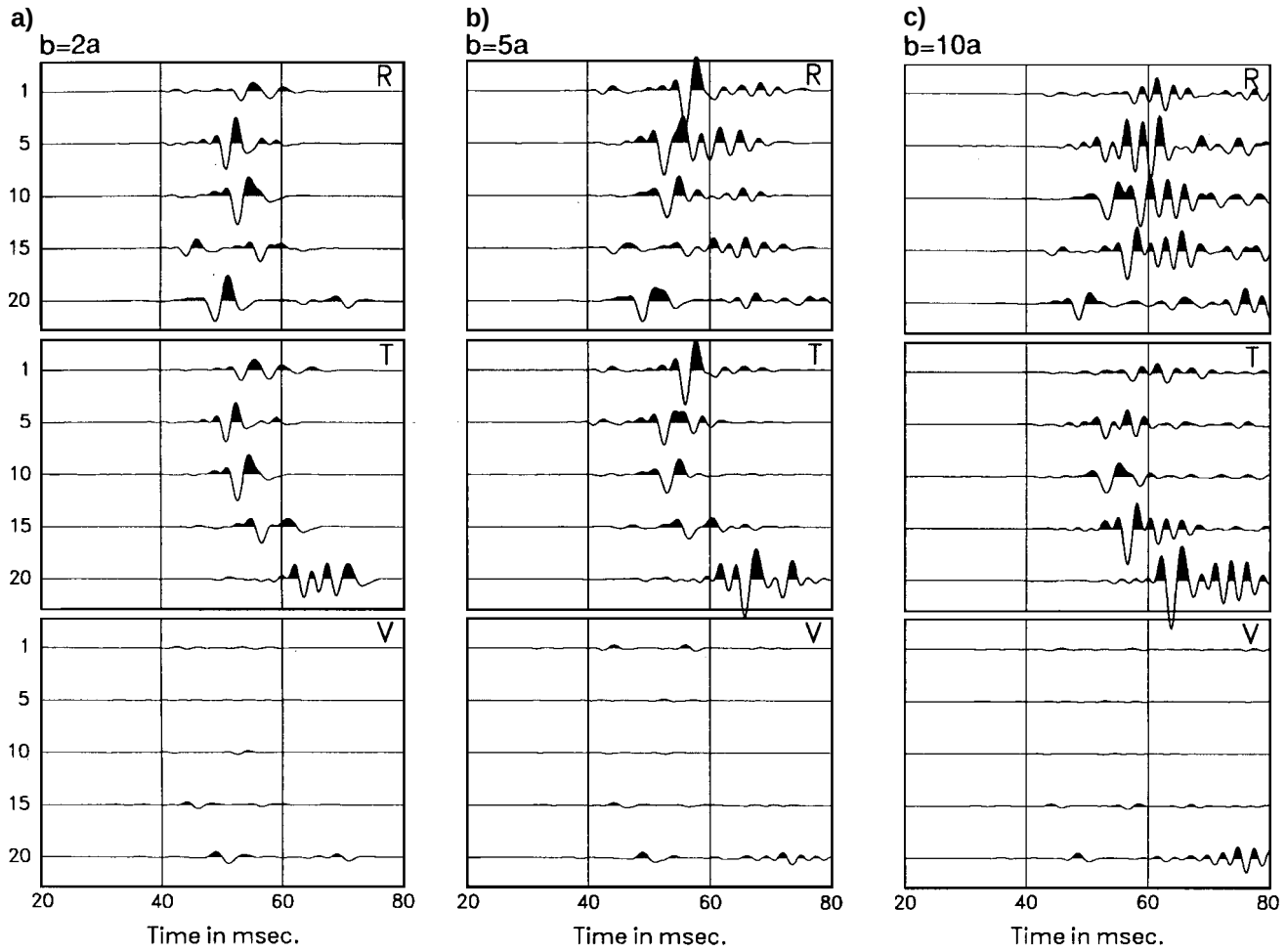

FIG. 6. Synthetic scattered waveforms computed for an elliptical crack (model geometry shown in Figure 2) with half-lengths indicated at the top of the plot (a is the short axis, and b is the long axis out of plane). The numbers on the left correspond to the geophone positions in Figure 2.

of 250 m. The amplitudes of the scattered waves change very little, and by matching the phases we obtain a best model for the height of around 56 to 72 m (traces 4 to 6 in Figure 12), which roughly agrees with the previously estimated height of 66 m. This is in contrast to Meadows and Winterstein, who obtain half the predicted length and almost require double the predicted height. The modeling results from their study and our own work are summarized as follows:

Our result:

$$1.5L_{\text{predicted}} \leq L_{\text{modeled}} \leq 2L_{\text{predicted}},$$

and

$$H_{\text{modeled}} \approx H_{\text{predicted}}$$

Meadows and Winterstein's result:

$$L_{\text{modeled}} \leq 0.5L_{\text{predicted}},$$

and

$$H_{\text{predicted}} \leq H_{\text{modeled}} \leq 2H_{\text{predicted}}.$$

In the above, H_{modeled} and L_{modeled} are the fracture height and length found by matching the observed diffracted wavelets. Our model does not require a significant adjustment of the estimated fracture height, but does require a slightly longer length. Note that in Figures 10 to 12, the scattered *SH*-waves (polarized parallel to the fracture) are negligible. This is due to the observation geometry and scattered radiation pattern and is not an intrinsic feature of the scattered *SH*-waves.

Implications for time-dependent changes in wavelets

Our results and those of Meadows and Winterstein provide strong evidence that the induced hydraulic fracture is responsible for the observed residual waves. Both the amplitudes and phases were matched reasonably well using the Kirchhoff approximation. Our final preferred model requires a fracture length of about 1.1 to 1.5 times the predicted length, while the fracture height is approximately the same as previously estimated from radioactive tracers (Meadows and Winterstein). These results differ from those obtained by Meadows and Winterstein, who require a short fracture length to match the phases. Meadows and Winterstein stated that the phase differences are not sensitive enough to determine the fracture sizes (length and height) with much confidence. However, by simultaneously matching the amplitudes

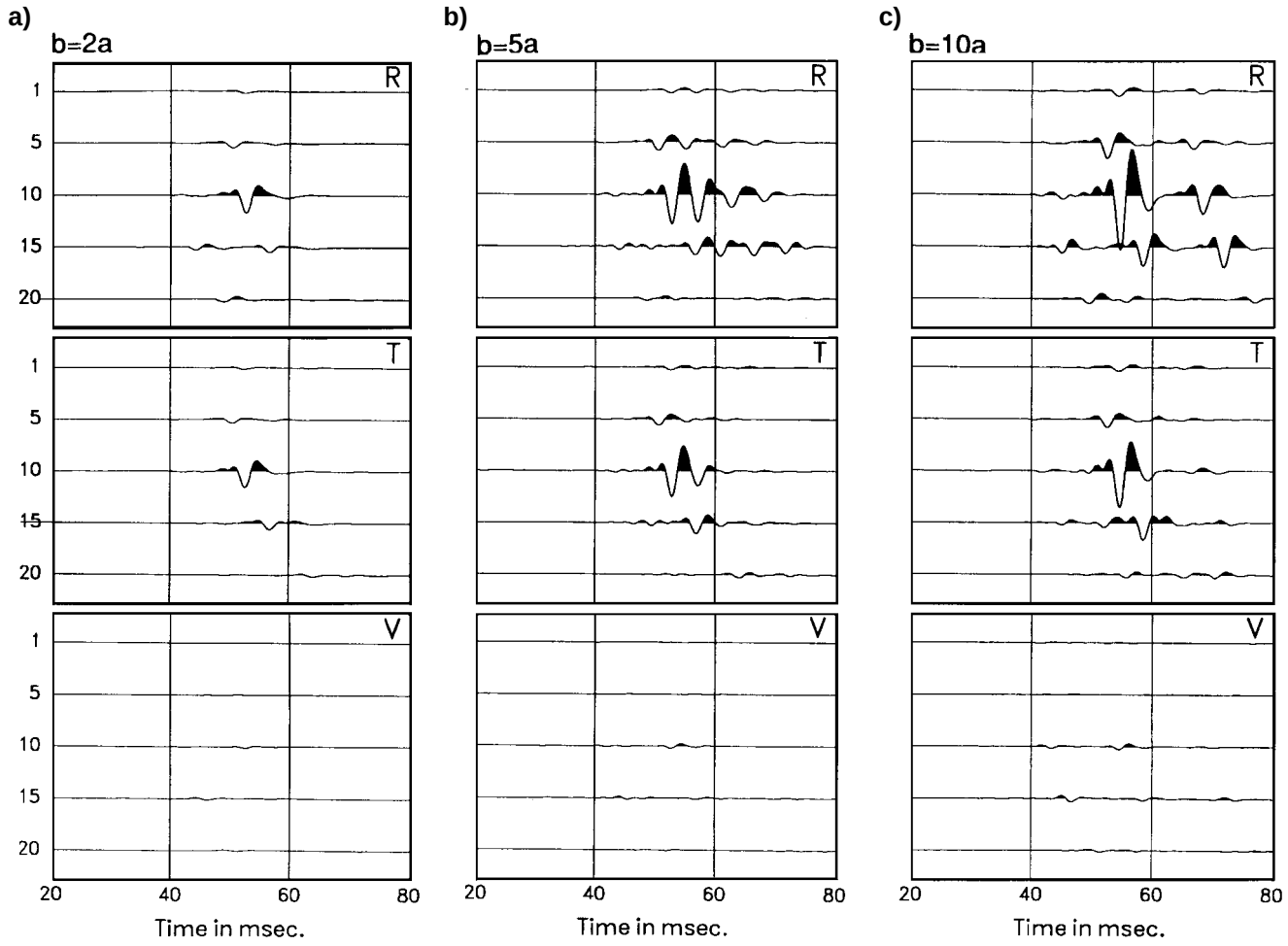

FIG. 7. Synthetic scattered waveforms computed for a rectangular crack (model geometry shown in Figure 2) with half-lengths indicated at the top of the plot (*a* is the short axis, and *b* is the long axis out of plane). The numbers on the left correspond to the geophone positions in Figure 2.

and phases, we have more constraints in the modeling. To make full use of this relatively new method in estimating the fracture dimensions, it is desirable to have a range of observations that provide a good angular coverage to obtain an accurate model.

It is interesting to note that the relative amplitudes of the two peaks of the synthetic scattered wavelets vary with the size of the fractures (Figures 11 to 12). This is particularly obvious in Figure 11, which shows the synthetic scattered wavelets for different fracture heights. We see that the amplitudes of the first peak gradually increase with increasing fracture height, whereas the amplitudes of the second peak change more dramatically. This feature is similar to the observed variation of scattered wavelets with time (Figure 9). The synthetic seismograms thus reveal that diffracted waves are sensitive to changes in fracture size.

Our modeling can also address the fracture closure process. The signals observed during the collapse of the fracture show a decrease in the amplitudes without significant change in the waveforms. Since we have shown that the scattered waveforms depend most strongly on the fracture length, the decrease in amplitude suggests that the hydraulic fracture collapsed perhaps by diffusion or leakoff along the whole of crack face, so that its aperture decreased while retaining the same length, rather than closing sequentially from the ends of the fracture.

CONCLUSIONS

In this paper, we have studied the seismic response of single cracks using synthetic and field data examples. The theory developed for the scattering of elastic waves by cracks and fractures is numerically evaluated. The synthetic results calculated for waves scattered from a single crack display a rich variety of informative phenomena, some of which have been briefly investigated in this study. The results strongly depend upon the distance of the observation point from the scattering object (crack), the incident wavelength, and the type of wave polarization. Within the shadow zone, the waves that dominate the solution near the crack are quite different from those that dominate at larger distances.

We have demonstrated that by matching observed waveform characteristics (phases and amplitudes) of diffracted waves, it is possible to gain an estimate of fracture dimensions when diffracted waves are accurately recorded, as in the Meadows and Winterstein (1994) experiment. Even when diffracted waves cannot be separated (or isolated), matching the full

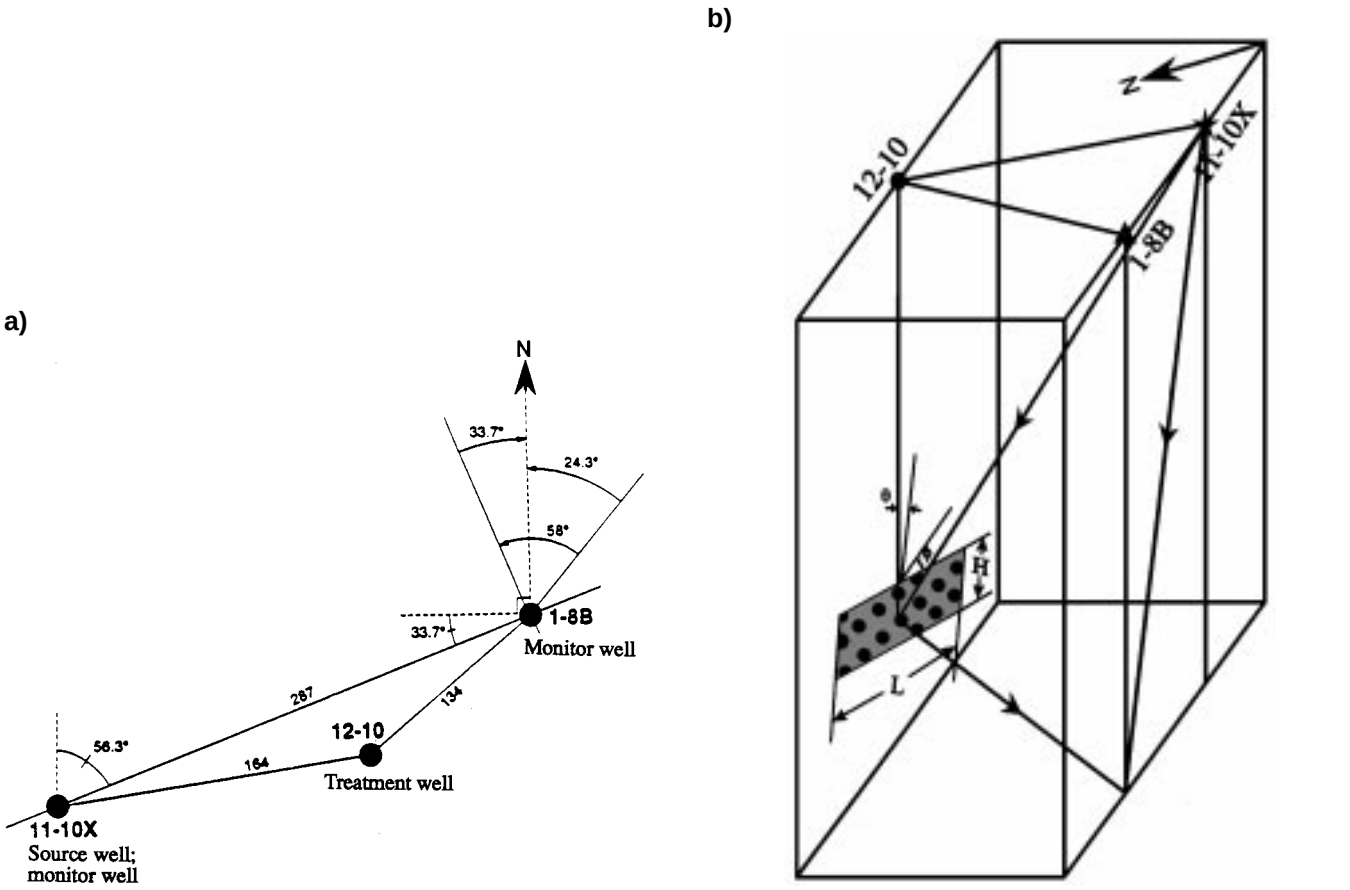

FIG. 8. (a) Plan view of the Lost Hills experiment (modified from Meadows and Winterstein, 1994). (b) Schematic illustration of the 3-D configuration of the source, geophones, and expected fracture positions in the field experiment (not to scale). H and L denote the fracture height and length, respectively. Here, θ and ϕ represent the fracture inclination (from vertical) and azimuth (from the direction between boreholes 1-8B and 11-10X), respectively.

waveform may still be possible, but this is probably less accurate since diffracted waves are usually much smaller than direct waves and are hidden in the coda of the direct waves.

Our modeled fracture length seems relatively large in comparison to previously published results, although the corresponding height matches agree well with the predicted propped height. One should, however, be cautious in placing too much faith in the modeling results. As indicated by Meadows and Winterstein, a rectangular area representation of a hydraulic fracture may be oversimplistic; in reality the hydraulic fracture is certainly not uniform and does not have the same opening everywhere. A more realistic hydraulic fracture model may look like an elliptical disturbed area, or more likely two elliptical disturbed areas placed symmetrically about the borehole axis (W. D. Rizer and J. H. Queen, Pers. Comm.). Modeling such fractures would be useful if several raypaths

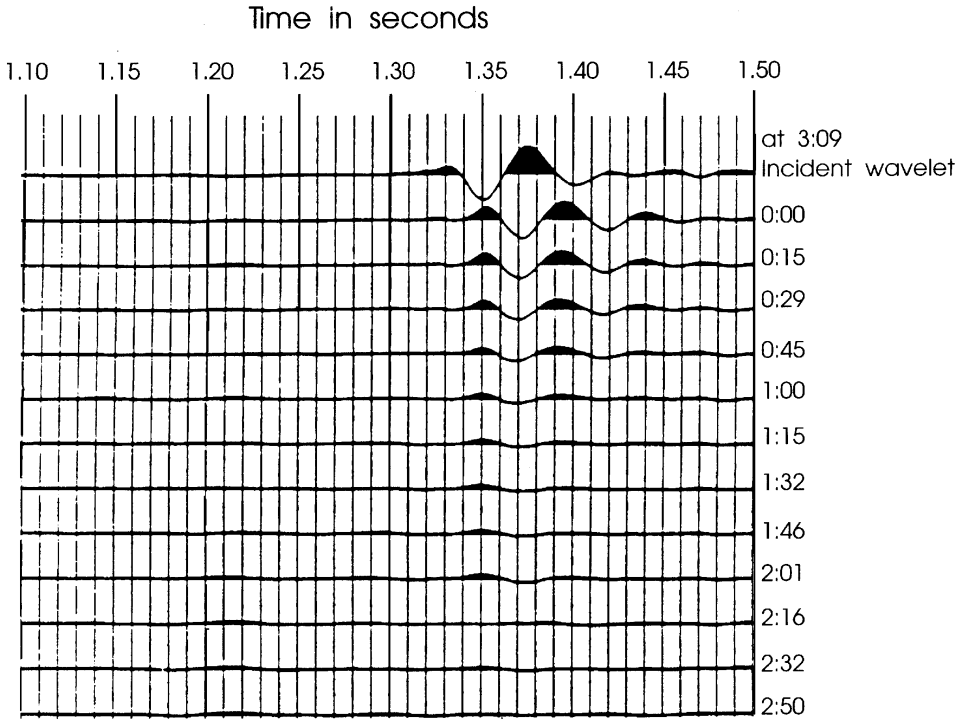

FIG. 9. Observed diffracted wavefield from the XX-component (SV-waves) after subtracting the last recorded trace, assumed to be the incident wavelet, from each of the other wavelets (modified from Meadows and Winterstein, 1994).

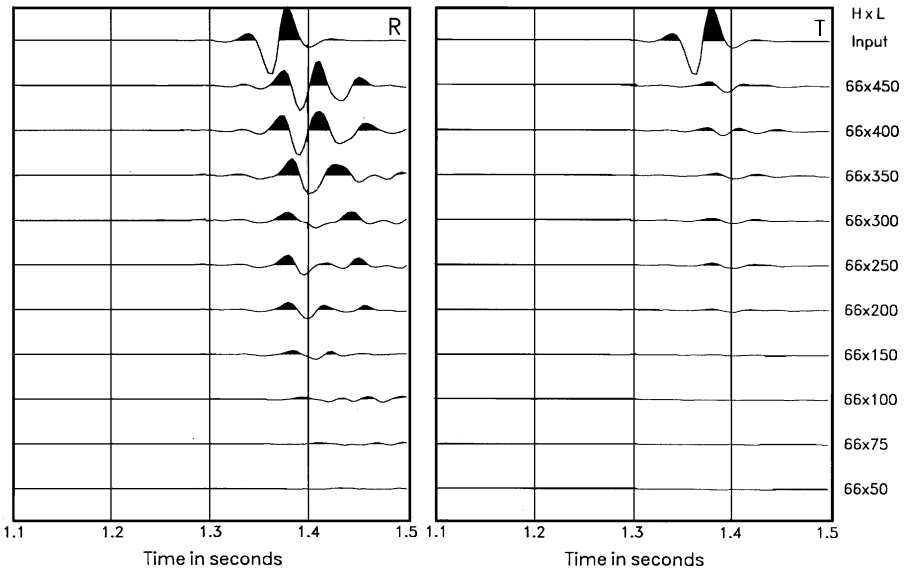

FIG. 10. Modeled scattered waveforms of SV-waves (XX-components) and SH-waves (YY-components) (labeled R and T, respectively) for various fracture lengths given on the right side of the plot with a fixed height. The length (L) and height (H) are given in meters on the right-hand side of the plot. The first trace is the input wavelet. The fracture is parallel to the plane containing the source and receiver; true fracture dip and true orientation were not considered.

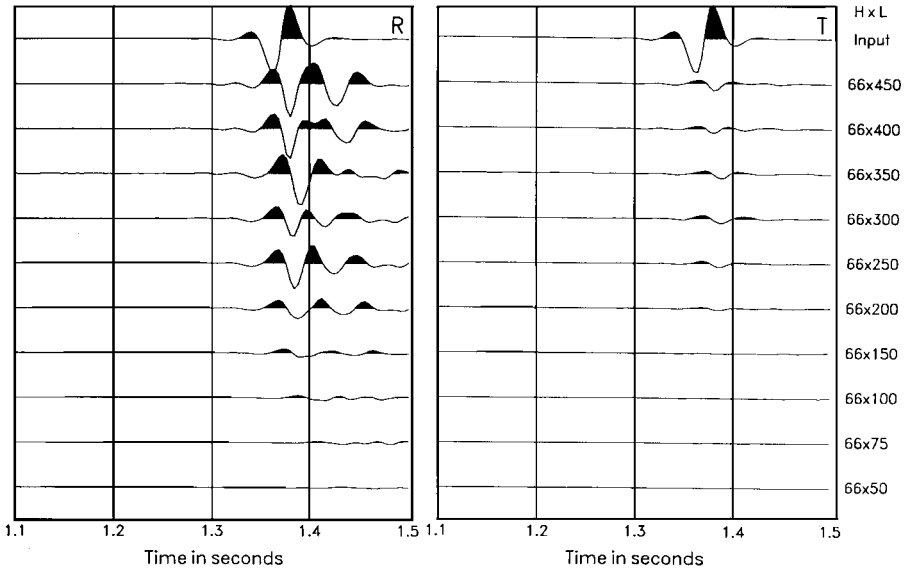

FIG. 11. Same as Figure 10, but with true fracture dip and orientation (see Table 3 of Meadows and Winterstein, 1994).

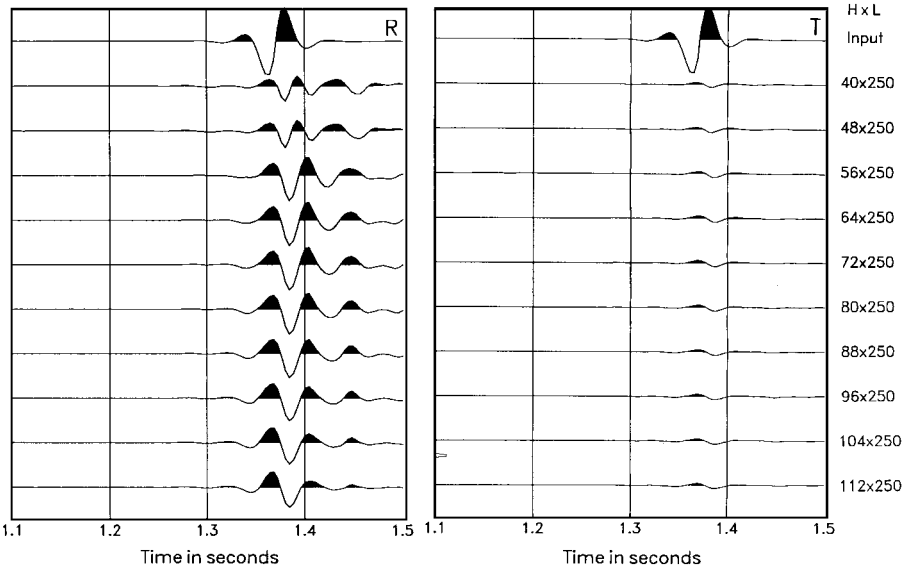

FIG. 12. Same as Figure 9, but for various fracture heights given on the right side of the plot and at a fixed fracture length.

are available so that an accurate picture of the fracture may be obtained. Nevertheless, we have demonstrated that the limit and extent of fracture can be established through matching observed waveforms, and in this sense our modeling is successful.

ACKNOWLEDGMENTS

We are grateful to Mark Meadows and Don Winterstein of Chevron for useful discussion about their field data and for detailed comments (by M. Meadows) on this paper. We thank John Queen and Bill Rizer of Conoco for useful discussion and comments during all stages of this project, and David Booth, Colin MacBeth, Tim Pointer, and Phil Wild of BGS for their comments on the manuscript. We also thank R. L. Brown, K. D. Mahrer (Associate Editor), and an anonymous reviewer for their detailed comments and criticisms that have greatly improved the readability of this paper. This work was supported by Conoco (UK) Limited through contract no. 2.343, and the Natural Environment Research Council of UK, and is published with the approval of Conoco (UK) Limited and the Director of the British Geological Survey (NERC).

REFERENCES

Achenbach, J. D., Gautesen, A. K., and McMaken, H., 1982, Ray methods for waves in elastic solids, with application to scattering by cracks: Pitman Learning.

Aki, K., and Richards, P. G., 1980, Quantitative seismology: theory and methods: W. H. Freeman & Co.

Chen, G., and Zhou, H., 1994, Boundary element modeling of nondispersive and dispersive waves: Geophysics, **59**, 113–118.

Coutant, O., 1989, Numerical study of the diffraction of elastic waves by fluid-filled cracks: J. Geophys. Res., **94**, 17 805–17 818.
Crampin, S., 1985, Evaluation of anisotropy by shear-wave splitting: Geophysics, **50**, 142–152.
Douglas, A., and Hudson, J. A., 1990, The effect on teleseismic *P* of the zone of damage created by an explosion: Geophys. J. Internat., **103**, 111–133.
Fehler, M., and Aki, K., 1978, Numerical study of diffraction of plane elastic waves by a finite crack with application to location of a magma lens: Bull. Seis. Soc. Am., **68**, 573–598.
Fehler, M., and Pearson, C., 1984, Crosshole seismic survey: application for studying subsurface fracture systems at a hot dry rock geothermal site: Geophysics, **49**, 37–45.
Geertsma, J., and deKlerk, F., 1969, A rapid method of predicting width and extent of hydraulically induced fracture: J. Petr. Tech., **21**, 1571–1581.
Gu, B., Nihei, K. T., Myer, L. R., and Pyrak-Nolte, L. J., 1996, Fracture interface waves: J. Geophys. Res., **101**, 827–835.
Hudson, J. A., 1980, The excitation and propagation of elastic waves: Cambridge Univ. Press.
Hudson, J. A., and Heritage, J. R., 1981, The use of Born approximation in seismic scattered problems: Geophys. J. Roy. Astr. Soc., **66**, 221–240.
Hudson, J. A., Liu, E., and Crampin, S., 1996, Reflection and diffraction from a bounded fault: Geophys. J. Internat., in press.
Liu, E., Hudson, J. A., Crampin, S., Rizer, W. D., and Queen, J. H., 1995, Seismic properties of a general fracture, *in* Rossmanith, H. P., Mechanics of jointed and faulted rocks: A. A. Balkema, 673–678.
Meadows, M., and Winterstein, D., 1994, Seismic detection of a hydraulic fracture from shear-wave VSP data at Lost Hills Field, California: Geophysics, **57**, 11–26.
Niitsuma, H., and Saito, H., 1991, Evaluation of the three-dimensional configuration of a subsurface artificial fracture by the triaxial shear shadow method: Geophysics, **56**, 2118–2128.
Press, W. H., Teukolsky, S. A., Vetterling, W. T., and Flannery, B. P., 1992, Numerical recipes: the art of scientific computing: Cambridge Univ. Press.
Pyrak-Nolte, L. J., Myer, L. R., and Cook, N. G. W., 1990, Transmission of seismic waves across single natural fractures: J. Geophys. Res., **95**, 8617–8638.
Raynaud, B., 1988, Diffraction modeling of 3-D lower crustal reflectors: Geophys. J. Internat., **93**, 149–161.
Tatham, R. H., and McCormack, M. D., 1991, Multicomponent seismology in petroleum exploration: Soc. Expl. Geophys.
van der Hijden, J. H. M. T., and Neerhoff, F. L., 1984a, Scattering of elastic waves by a plane crack of finite width: J. App. Mech., **51**, 646–651.
——— 1984b, Diffraction of elastic waves by a subsurface crack (in-plane motion): J. Accost. Soc. Am., **75**, 1694–1704.
Vinegar, H. J., Willis, P. B., DeMartini, D. C., Shlyapobersky, J., Deeg, W. F. J., Adair, R. G., Woerpel, J. C., Fix, J. E., and Sorrells, G. G., 1992, Active and passive seismic imaging of a hydraulic fracture in diatomite: J. Petr. Tech., **44**, 28–34 and 88–90.
Wills, P. B., DeMartini, D. C., Vinegar, H. J., Shlyapobersky, J., Deeg, W. F. J., Adair, R. G., Woerpel, J. C., Fix, J. E., and Sorrells, G. G., 1992, Active and passive imaging of hydraulic fractures: The Leading Edge, **11**, No. 7, 15–22.
Wu, R. S., and Aki, K., 1985, Scattering characteristics of elastic waves by an elastic heterogeneity: Geophysics, **50**, 582–589.

APPENDIX

DERIVATION OF DISPLACEMENT DISCONTINUITIES

In equations (8) and (9), we give the scattered radiation of plane-wave response for a *P*- and *S*-wave scattered by a crack. The key step is the calculation of the jump in displacement, or the crack opening displacement $[\mathbf{u}] = \mathbf{u}_2 - \mathbf{u}_1$, where $\mathbf{u}_2$ and $\mathbf{u}_1$ are the displacements across a fracture. If the incident wave is a plane wave (neglecting the time-dependent term),

$$\mathbf{u}^0 = \mathbf{q} \cdot e^{i\mathbf{k}\cdot\mathbf{x}}, \tag{A-1}$$

where $\mathbf{k} = \mathbf{n}\omega/v$ is the wavenumber vector, v is the *P*- or *S*-wave velocity, and ω is the frequency. $\mathbf{n}\cdot\mathbf{q} = 1$ for *P*-waves, and $\mathbf{n}\cdot\mathbf{q} = 0$ for *S*-waves. In the local coordinate system, where the raypaths lie in the *x*-*z* plane and the fracture in the *x*-*y* plane, the unit propagation vector $\mathbf{n} = (\sin\theta, 0, \cos\theta)$, we have the polarization vector $\mathbf{q} = (\sin\theta, 0, \cos\theta)$ for *P*-waves, $\mathbf{q} = (\cos\theta, 0, -\sin\theta)$ for *SV*-waves, and $\mathbf{q} = (0, 1, 0)$ for *SH*-waves, where θ is the incident angle with respect to the fracture normal, i.e., the *z*-axis. The Kirchhoff approximation consists of replacing $[\mathbf{u}]$ by the values it would have if the fracture were not bounded; that is the equivalent discontinuity on an unbounded fracture plane. The approximation to $[\mathbf{u}]$ takes the form

$$[\mathbf{u}] = \mathbf{Q} \cdot e^{i\mathbf{k}\cdot\mathbf{X}}, \tag{A-2}$$

for points $\mathbf{X}$ on the fracture plane, where $\mathbf{Q}$ is independent of $\mathbf{X}$.

SH-wave incidence

In the case of *SH*-wave incidence, $\mathbf{q} = (0, q_2, 0)$ and $\mathbf{u}_0 = (0, q_2, 0)\, e^{i\mathbf{k}\cdot\mathbf{x}}$, and the reflected *SH*-wave is then given by

$$\mathbf{u}^r = (0, q_2, 0)\, R_{SH} e^{i\mathbf{k}\cdot\mathbf{x}}, \tag{A-3}$$

and the transmitted *SH*-wave is given by

$$\mathbf{u}^t = (0, q_2, 0)\, T_{SH} e^{i\mathbf{k}\cdot\mathbf{x}}, \tag{A-4}$$

where R_{SH} and T_{SH} are the plane *SH*-wave reflection and transmission coefficients, respectively. If we assume that the horizontal fracture is in the $z = 0$ plane, we have

$$[u_1]|_{x_1=0,x_3=0} = [u_3]|_{x_1=0,x_3=0} = 0, \tag{A-5}$$

$Q_1 = Q_3 = 0$, and

$$[u_2]|_{x_3=0} = u_2^t - \left(u_2^r + u_2^0\right)\big|_{x_3=0} = Q_2, \tag{A-6}$$

so we have

$$Q_2 = T_{SH} - (R_{SH} + q_2). \tag{A-7}$$

Equation (A-7) can be simplified further. Using the analytic expressions for T_{SH} and R_{SH} given by Pyrak-Nolte et al. (1990),

$$T_{SH} = \frac{2K_y}{(2K_y - i\mu k_3)}, \tag{A-8}$$

and

$$R_{SH} = \frac{-i\mu k_3}{(2K_y - i\mu k_3)}, \tag{A-9}$$

equation (A-7) then becomes

$$Q_2 = \frac{-2}{[1 + 2iK_y/\mu k_3]}, \tag{A-10}$$

where K_y is the fracture stiffness, μ is the shear modulus, k_3 is the vertical wavenumber $[k_3 = (\omega/\beta)\cos(\theta)]$, θ is the angle of incidence, and we assume $q_2 = 1$. The alternative derivation of equation (A-10) is by direct use of the formula $[u_2] = (1/K_y)\tau_2$ (see Liu et al., 1995; Pyrak-Nolte et al., 1990), where $\tau_2 = \sigma_{23}$ is the component of stress.

***P-SV* wave incidence**

In the following section, we shall consider the SV-wave only; the derivation of $\mathbf{Q}$ for the P-wave follows the same procedure. We have $\mathbf{q} = (q_1, 0, q_3)$ and $\mathbf{u}^0 = (q_1, 0, q_3)\, e^{i\mathbf{k}\cdot\mathbf{x}}$. The reflected P- and SV-waves are given by

$$ {}^{P}\mathbf{u}^{r} = (\sin\theta_1, 0, -\cos\theta_1) R_{SVP}\, e^{i\mathbf{k}\cdot\mathbf{x}}, \tag{A-11} $$

and

$$ {}^{S}\mathbf{u}^{r} = (\cos\phi_1, 0, \sin\phi_1) R_{SVSV}\, e^{i\mathbf{k}\cdot\mathbf{x}}, \tag{A-12} $$

and the transmitted P- and SV-waves are

$$ {}^{P}\mathbf{u}^{t} = (\sin\theta_2, 0, \cos\theta_2) T_{SVP}\, e^{i\mathbf{k}\cdot\mathbf{x}}, \tag{A-13} $$

and

$$ {}^{S}\mathbf{u}^{t} = (\cos\phi_2, 0, -\sin\phi_2) T_{SVSV}\, e^{i\mathbf{k}\cdot\mathbf{x}}, \tag{A-14} $$

where R and T are the appropriate reflection and transmission coefficients for plane P- and SV-waves. θ and ϕ are the incidence angles of the P- and SV-waves, respectively. The displacement discontinuity boundary condition does not influence the emergence angles θ_2 and ϕ_2 which are related to the incident angles θ_1 and ϕ_1 by Snell's law:

$$ \frac{\alpha_1}{\sin\theta_1} = \frac{\alpha_2}{\sin\theta_2} = \frac{\beta_1}{\sin\phi_1} = \frac{\beta_2}{\sin\phi_2}, \tag{A-15} $$

where α_1, β_1, and α_2 and β_2 are P- and S-velocities of the medium surrounding the cracks, respectively. Again assuming the fracture is in the $z = 0$ plane, we have

$$ [\mathbf{u}]|_{x_1=0, x_3=0} = ({}^{P}\mathbf{u}^{t} + {}^{S}\mathbf{u}^{t}) - ({}^{P}\mathbf{u}^{r} + {}^{S}\mathbf{u}^{r} + \mathbf{u}^{0})|_{x_1=0, x_3=0} = \mathbf{Q}. \tag{A-16} $$

Substituting equations (A-11) to (A-14) into equation (A-16) and after some simple algebra, we can obtain the expressions for $\mathbf{Q}$ in terms of the reflection and transmission coefficients:

$$ Q_1 = [T_{SVP}\sin\theta_2 + T_{SVSV}\cos\phi_2] - [R_{SVP}\sin\theta_1 + R_{SVSV}\cos\phi_1 + q_1], \tag{A-17} $$

and

$$ Q_3 = [T_{SVP}\cos\theta_2 - T_{SVSV}\sin\phi_2] - [-R_{SVP}\cos\theta_1 + R_{SVSV}\sin\phi_1 + q_3], \tag{A-18} $$

and $Q_2 = 0$. Similarly, for P-wave incidence, we have

$$ Q_1 = [T_{PP}\sin\theta_2 + T_{PSV}\cos\phi_2] - [R_{PP}\sin\theta_1 + R_{PSV}\cos\phi_1 + q_1], \tag{A-19} $$

and

$$ Q_3 = [T_{PP}\cos\theta_2 - T_{PSV}\sin\phi_2] - [-R_{PP}\cos\theta_1 + R_{PSV}\sin\phi_1 + q_3], \tag{A-20} $$

and $Q_2 = 0$. The reflection (R) and transmission (T) coefficients are the solutions of 4×4 linear equations (see for example, Pyrak-Nolte et al., 1990), which are in very complicated forms (although analytic solutions can be obtained in theory and are evaluated numerically).